INTERNATIONAL JOURNAL FOR NUMERICAL METHODS IN FLUIDS
Int. J. Numer. Meth. Fluids 2006; **51**:1177–1203
Published online 14 March 2006 in Wiley InterScience (www.interscience.wiley.com). DOI: 10.1002/fld.1211

Convergence study of a family of flux-continuous, finite-volume schemes for the general tensor pressure equation

Mayur Pal*,†, Michael G. Edwards‡ and Anthony R. Lamb§

Civil and Computational Engineering Centre, School of Engineering, University of Wales Swansea, Singleton Park Swansea, SA2 8PP Wales, U.K.

SUMMARY

In this paper, a numerical convergence study of family of flux-continuous schemes is presented. The family of flux-continuous schemes is characterized in terms of quadrature parameterization, where the local position of continuity defines the quadrature point and hence the family. A convergence study is carried out for the discretization in physical space and the effect of a range of quadrature points on convergence is explored. Structured cell-centred and unstructured cell-vertex schemes are considered. Homogeneous and heterogeneous cases are tested, and convergence is established for a number of examples with discontinuous permeability tensor including a velocity field with singularity. Such cases frequently arise in subsurface flow modelling. A convergence comparison with CVFE is also presented. Copyright © 2006 John Wiley & Sons, Ltd.

KEY WORDS: convergence; flux continuous; discontinuous coefficients; quadrature and pressure equation

1. INTRODUCTION

Rapid variation in permeability is common in oil reservoirs where permeability coefficients can jump by several orders of magnitude. Continuity of flux and pressure at local physical interfaces between grid blocks with strong discontinuities in permeability are fundamental laws that must be built into the discrete scheme approximation of the pressure equation.

A family of flux-continuous, locally conservative, finite volume schemes has been developed for general geometry-permeability tensor pressure equation, on structured and unstructured grids [1–8]. In these schemes discrete flow variables and rock properties including permeability

*Correspondence to: Mayur Pal, Civil and Computational Engineering Centre, School of Engineering, University of Wales Swansea, Singleton Park Swansea, SA2 8PP Wales, U.K.
†E-mail: 339620@swan.ac.uk
‡E-mail: m.g.edwards@swansea.ac.uk
§E-mail: a.lamb@swansea.ac.uk

Received 3 June 2005
Revised 12 January 2006
Accepted 18 January 2006

tensors are assigned to control-volumes so that the schemes are control-volume distributed or CVD. Flux-continuous schemes are also presented in References [9–14] where they are called as multi-point flux approximation schemes or MPFA. Similar schemes are also presented in References [15, 16]. The schemes are applicable to the diagonal and full tensor pressure equation with generally discontinuous coefficients and remove the $O(1)$ error introduced by standard reservoir simulation schemes when applied to full tensor flow approximation. Mixed finite element methods and discontinuous Galerkin have also been developed for the flow in porous media, e.g. References [17–21].

This paper addresses the numerical convergence for the family of flux-continuous schemes developed by Edwards and Rogers [1] in physical space [3, 4] for a range of quadrature points. The underlying principle of the family of flux-continuous schemes is the continuity of normal flux and pressure. Advantages of the family of flux-continuous schemes in terms of sensitivity to cross-flow and improved performance were noted in References [5, 22]. In this paper, results are presented for a number of cases and numerical convergence of the scheme is presented. It is also shown how the use of specific quadrature points improves the convergence of the numerical scheme. Earlier results have been presented for numerical convergence of the basic MPFA O-method (which is one of the family of flux-continuous schemes) on general quadrilateral grids in transform [1] and physical space [14]. The numerical schemes for the convergence study are presented here using a cell-centred CVD formulation for quadrilateral grids and a cell-vertex polygonal CVD formulation for unstructured grids.

This paper is organized as follows: Section 2 gives a description of the single phase flow problem encountered in reservoir simulation with respect to general tensor pressure equation. Section 3 presents an overview of the flux-continuous formulation starting in 1-D followed by classical five-point scheme in 2D and the generalization of the flux-continuous scheme for structured and unstructured grids, with discretization of the scheme in *physical* space. Section 3 also reviews the family of flux-continuous schemes and the effects of using different quadrature points. Section 4 presents the numerical convergence results for the family of schemes for a range of quadrature points with the help of a series of numerical examples with varying degrees of roughness coefficients. In Section 5 convergence of the family of flux-continuous schemes is considered in terms of an up-scaling example on structured and unstructured grids. Section 4 presents the conclusion of the convergence study.

2. THE PROBLEM DEFINITION

2.1. Cartesian tensor

The problem is to find the pressure ϕ satisfying

$$-\int_{\Omega} \nabla \bullet \mathbf{K}(x, y)\nabla\phi \, \mathrm{d}\tau = \int_{\Omega} q \, \mathrm{d}\tau = m \tag{1}$$

over an arbitrary domain Ω, subjected to suitable (Neumann/Dirichlet) boundary conditions on boundary $\partial\Omega$. The right-hand side term m represents a specified flow rate and $\nabla = (\partial_x, \partial_y)$.

Matrix $\mathbf{K}$ can be a diagonal or full Cartesian tensor with general form

$$\mathbf{K} = \begin{pmatrix} K_{11} & K_{12} \\ K_{12} & K_{22} \end{pmatrix} \tag{2}$$

The full tensor pressure equation is assumed to be *elliptic* such that

$$K_{12}^2 \leqslant K_{11}K_{22} \tag{3}$$

The tensor can be discontinuous across internal boundaries of Ω. The boundary conditions imposed here are Dirichlet and Neumann. For incompressible flow pressure is specified at atleast one point in the domain. For reservoir simulation, Neumann boundary conditions on $\partial\Omega$ requires zero flux on solid walls such that $(K\nabla\phi)\cdot\hat{n} = 0$, where $\hat{n}$ is the outward normal vector to $\partial\Omega$.

2.2. General tensor equation

The pressure equation is defined above with respect to the *physical* tensor in the initial classical Cartesian co-ordinate system. Now we proceed to a general curvilinear co-ordinate system that is defined with respect to a uniform dimensionless transform space with a (ξ, η) co-ordinate system. Choosing Ω_p to represent an arbitrary control-volume comprised of surfaces that are tangential to constant (ξ, η), respectively, Equation (1) is integrated over Ω_p via the Gauss divergence theorem to yield

$$-\oint_{\partial\Omega_p} (\mathbf{K}\nabla\Phi)\cdot\hat{\mathbf{n}}\,\mathrm{d}s = \mathbf{M} \tag{4}$$

where $\partial\Omega_p$ is the boundary of Ω_p and $\hat{n}$ is the unit outward normal. Spatial derivatives are computed using

$$\phi_x = J(\phi, y)/J(x, y), \phi_y = J(x, \phi)/J(x, y) \tag{5}$$

where $J(x, y) = x_\xi y_\eta - x_\eta y_\xi$ is the Jacobian. Resolving the x, y components of velocity along the unit normals to the curvilinear co-ordinates (ξ, η), e.g. for $\xi = \text{constant}$, $\hat{\mathbf{n}}\,\mathrm{d}s = (y_\eta, -x_\eta)\,\mathrm{d}\eta$ gives rise to the general tensor flux components

$$F = -\int (T_{11}\phi_\xi + T_{12}\phi_\eta)\,\mathrm{d}\eta, \quad G = -\int (T_{12}\phi_\xi + T_{22}\phi_\eta)\,\mathrm{d}\xi \tag{6}$$

where general tensor $\mathbf{T}$ has elements defined by

$$\begin{aligned} T_{11} &= (K_{11}y_\eta^2 + K_{22}x_\eta^2 - 2K_{12}x_\eta y_\eta)/J \\ T_{22} &= (K_{11}y_\xi^2 + K_{22}x_\xi - 2K_{12}x_\xi y_\xi)/J \\ T_{12} &= (K_{12}(x_\xi y_\eta + x_\eta y_\xi) - (K_{11}y_\eta y_\xi + K_{22}x_\eta x_\xi))/J \end{aligned} \tag{7}$$

and the closed integral can be written as

$$\iint_{\Omega_p} \frac{(\partial_\xi\tilde{F} + \partial_\eta\tilde{G})}{J} J\,\mathrm{d}\xi\,\mathrm{d}\eta = \triangle_\xi F + \triangle_\eta G = m \tag{8}$$

where, e.g. $\triangle_\xi F$ is the difference in net flux with respect to ξ and $\tilde{F} = -(T_{11}\phi_\xi + T_{12}\phi_\eta)$, $\tilde{G} = -(T_{12}\phi_\xi + T_{22}\phi_\eta)$. Thus, any scheme applicable to a full tensor also applies to non-K-Orthogonal grids. Note that $T_{11}, T_{22} \geqslant 0$ and ellipticity of $\mathbf{T}$ follows from Equations (3) and (7). Full tensors can arise from up-scaling, and orientation of grid and permeability field. For example, by Equation (7), a diagonal anisotropic Cartesian tensor leads to a full tensor on a curvilinear *orthogonal* grid.

3. FLUX CONTINUOUS APPROXIMATION

The key to any finite volume formulation lies in working with the integral form of flow equations. The Gauss divergence theorem is applied locally to the volume integral of divergence over each control-volume. A unique discrete flux is then assigned to each control-volume face and each closed integral is approximated by sum of discrete outward normal fluxes. For a given face which is common to two neighbouring control-volumes, a unique flux is added to left-hand control-volume while the same flux is subtracted from the right-hand control-volumes leaving only the sum of global domain boundary fluxes. Thus, the flux-continuous schemes considered here are locally conservative. The construction of the flux-continuous scheme is given below.

3.1. Flux-continuous approximation in 1D

We begin with classical cell-centred formulation in one dimension where pressures and permeabilities are defined with respect to cell centres. In this case, Equation (1) reduces to

$$-\int (K(x)\phi_x)_x \, \mathrm{d}x = m \tag{9}$$

Integration of Equation (9) over the cell i (referring to Figure 1) results in the discrete difference of fluxes

$$F_{i+1/2} - F_{i-1/2} = m \tag{10}$$

where m is a flow rate, $F_{i+1/2} = -K\partial\phi/\partial x$ and the derivative remains to be defined. If the coefficient K is sufficiently smoothly varying it is possible to use linear interpolation between the centres of cells i and $i+1$ and approximates the flux by

$$F_{i+1/2} = -K_{i+1/2}(\phi_{i+1} - \phi_i)/\Delta x \tag{11}$$

where $K_{i+1/2}$ is a suitable average of the adjacent cell-centred permeabilities. However, if K is discontinuous then since normal flux and pressure are continuous the pressure gradient is

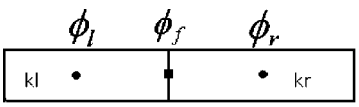

Figure 1. One-dimensional cell-centred and cell-face pressures.

discontinuous and linear interpolation is not valid across the cell faces. The standard solution to this problem is described in Reference [23]. Continuous pressure and normal flux are incorporated in the cell-centred approximation by introducing a mean pressure ϕ_f at a cell face dividing neighbouring cells (Figure 1). Equating the resulting one-sided flux approximation at the cell face results in

$$-K_r(\phi_r - \phi_f)/\Delta x_r = -K_l(\phi_f - \phi_l)/\Delta x_l \tag{12}$$

which ensures flux continuity. From Equation (12) cell-face pressure is given by

$$\phi_f = (\phi_l K_l/\Delta x_l + \phi_r K_r/\Delta x_r)/(K_l/\Delta x_l + K_r/\Delta x_r) \tag{13}$$

which is back-substituted into the discrete flux equation (12) to yield the classical cell-face flux approximation

$$F = -2K_r K_l(\phi_r - \phi_l)/(K_r \Delta x_l + K_l \Delta x_r) \tag{14}$$

3.2. Flux-continuous approximation in 2D classical five-point scheme

As in one dimension pressures and permeabilities have a cellwise distribution and cells act as control-volumes. The equivalent 2D discontinuous diagonal tensor five-point scheme on rectangular grid is derived by introduction of interface pressures and a sub-cell triangular support as indicated in Figure 2(a). As in one dimension cell-face pressures are eliminated in the flux continuity conditions to yield the classical five-point scheme with harmonic mean coefficients in two dimensions, further details of the scheme can be found in Reference [1]. The support for the classical five-point scheme is shown in Figure 2(b), and it shows that introduction of cell-face pressures ($\Phi_f = (\phi_N, \phi_S, \phi_E, \phi_W,)$) enables the normal velocity and pressure to be pointwise continuous at the cell faces.

3.3. Full tensor flux approximation

Continuous normal flux and pressure discretization of the reservoir simulation pressure equation is required in order to honour correct local physical interface conditions between grid

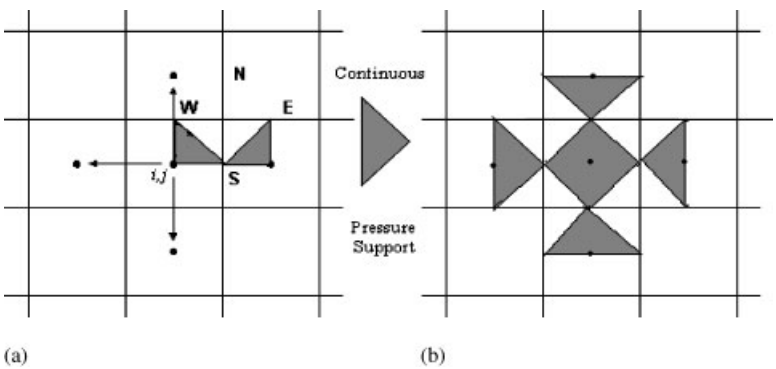

Figure 2. (a) Imposing continuity between the grid blocks in a five-point scheme; and (b) cell-centred five-point support on a Cartesian grid.

blocks with strong discontinuities in permeability. A consistent full tensor flux approximation requires an increase in support compared to the standard two-point flux. In general, a nine-point scheme is required for approximation of Equation (1) in two dimension as shown on a Cartesian or quadrilateral grids with full/diagonal tensor in Figures 3 and 4(a), respectively. Here we review the derivation of the family of flux-continuous schemes presented in References [1, 2]. Emphasis is on the comparison and benefits of different quadrature points (explained in Section 3.5 below) that belong to the family of flux-continuous schemes derived in physical space. There are multiple motivations for a family of schemes for both full and diagonal tensor formulations and these are stated below. This is followed by a presentation of the quadrature parameterization on which the schemes are based.

3.4. Motivation for the family of schemes

The motivation for the family of flux-continuous schemes and flexibility in location of quadrature point with $0 < q \leqslant 1$ is to allow for improvement in accuracy, e.g. $q = 1/2$ yields a significant gain in accuracy with order $O(h^6)$ truncation error for the Laplacian operator and $O(h^4)$ for an anisotropic diagonal tensor [1]. A nine-point scheme will also reduce grid orientation effects [22] and flux-continuous nine-point schemes can improve up-scaling even in

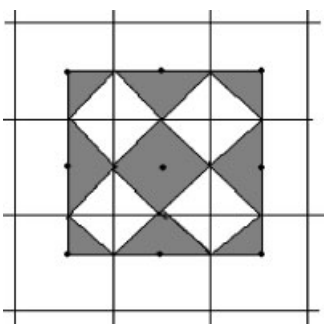

Figure 3. Full tensor pressure support with standard default quadrature point $q = 1$.

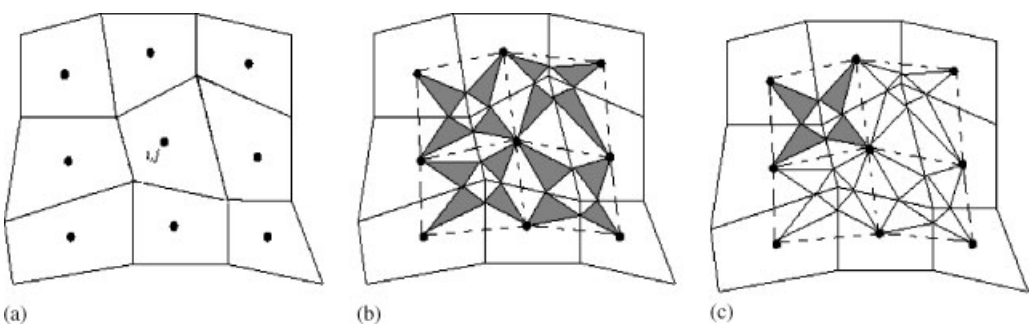

Figure 4. (a) Nine-point scheme support; (b) nine-point continuous pressure support shaded, quadrature $q = 1/2$; and (c) highlighted *dual-cell*.

the case of a diagonal tensor by detecting cross-flow [5]. Variable q can also improve diagonal dominance of the full tensor approximation [1].

3.5. Quadrature parameterization—physical space

The most primitive member of the family of schemes (illustrated in Figure 3) corresponds to the quadrature point position coincident with the cell-face mid-point, i.e. $q=1$. This is called *one-sided quadrature*, since, in this case, a diagonal tensor formulation will only involve two pressures from the four pressures $(\phi_{i,j}, \phi_{i+1,j}, \phi_{i+1,j+1}, \phi_{i,j+1})$, resulting in a two-point flux, and the basis functions reduce to right-angled triangles on a Cartesian grid. In this case, a six-point flux will only result when a full tensor is present. The general cell-centred flux-continuous schemes support is shown in Figure 4(a) with a nine-point support centred at i,j. A set of flux continuity conditions are imposed inside each dual-cell, where dual-cells are defined by joining cell centres to cell edge mid-points surrounding primal grid vertex as indicated by dashed lines in Figure 5(a). For a given *dual-cell*, the position of continuity can be chosen to lie at any point between the mid-point of a cell face and an adjacent grid cell vertex at the corner of the control-volume shown in Figure 5(b). The continuity position determines the scheme quadrature, consequently the co-ordinates of the continuity position N, S, E, W defines a whole family of flux-continuous nine-point schemes for a diagonal or full tensor equation. The co-ordinate system of a physical cell is illustrated in Figure 5, and is parameterized in terms of q $(0<q\leqslant 1)$, where the origin $(q=0)$ is the top right-hand corner of the cell and $q=1$ is the cell-face mid-point, and is given as, e.g.

$$\mathbf{r}=\mathbf{r}_3+\frac{q}{2}(\Delta\mathbf{r}_{23}) \tag{15}$$

where

$$\Delta\mathbf{r}_{23}=((x_2-x_3),(y_2-y_3)),\quad \mathbf{r}_2=(x_2,y_2),\quad \mathbf{r}_3=(x_3,y_3) \tag{16}$$

3.6. Formulation of scheme in physical space

Here, we now consider the full tensor flux approximation. Note that while normal flux is continuous across an interface tangential flux can be discontinuous. With respect to each *dual-cell* primal grid cell-face pressures $\Phi_{\mathrm{f}}=(\phi_{\mathrm{N}},\phi_{\mathrm{S}},\phi_{\mathrm{E}},\phi_{\mathrm{W}},)$ are introduced at the (N,S,E,W) locations indicated in Figure 6(a), and lie inside each *dual-cell*. A local triangular support is introduced within each quarter of the *dual-cell* (sub-cell) as shown in Figure 6(b). Pressure ϕ and the cell co-ordinates assume a piecewise linear variation over each triangle, for example, over the triangle of cell 1 (Figure 6(b))

$$\begin{aligned}\phi &= \xi\phi_{\mathrm{S}}+\eta\phi_{\mathrm{W}}+(1-\xi-\eta)\phi_1\\ x &= \xi x_{\mathrm{S}}+\eta x_{\mathrm{W}}+(1-\xi-\eta)x_1\\ y &= \xi y_{\mathrm{S}}+\eta y_{\mathrm{W}}+(1-\xi-\eta)y_1\end{aligned} \tag{17}$$

(ξ,η) are area co-ordinates and $(x_{\mathrm{S}},y_{\mathrm{S}})$, $(x_{\mathrm{W}},y_{\mathrm{W}})$ are local continuity co-ordinates and pressure is piecewise continuous over each triangle. The point of continuity on the cell face defines

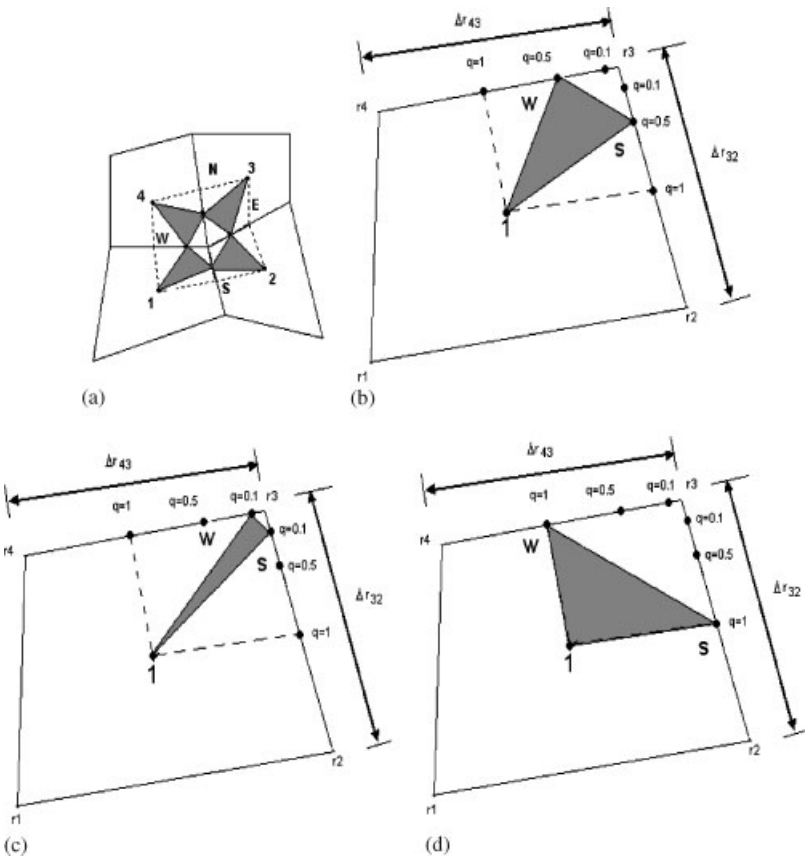

Figure 5. (a) Dual-cell—dashed line: flux and pressure continuity at N, S, E, W, quadrature $q = 1/2$; (b) local cell co-ordinate system with $q = 0.5$; (c) local cell co-ordinate system with $q = 0.1$; and (d) local cell co-ordinate system with $q = 1$.

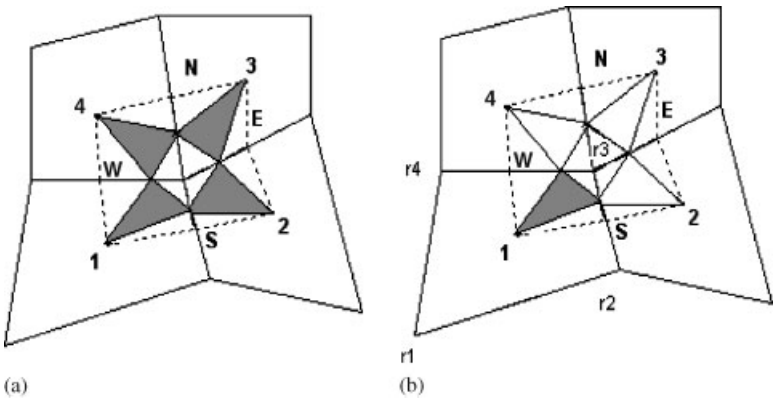

Figure 6. (a) Dual-cell—dashed line: flux and pressure continuity at N, S, E, W, quadrature $q = 1/2$; and (b) sub-cell of the dual-cell with pressure support.

the quadrature type. Sub-cell gradients are calculated using Equation (5) and (17) for triangle (1,S,W) leading to a well-known piecewise constant gradient in physical space where

$$\begin{pmatrix}\phi_\xi\\ \phi_\eta\end{pmatrix}=\begin{pmatrix}\phi_{\mathrm{S}}-\phi_1\\ \phi_{\mathrm{W}}-\phi_1\end{pmatrix} \tag{18}$$

and

$$\begin{pmatrix}x_\xi\\ x_\eta\end{pmatrix}=\begin{pmatrix}x_{\mathrm{S}}-x_1\\ x_{\mathrm{W}}-x_1\end{pmatrix},\quad \begin{pmatrix}y_\xi\\ y_\eta\end{pmatrix}=\begin{pmatrix}y_{\mathrm{S}}-y_1\\ y_{\mathrm{W}}-y_1\end{pmatrix} \tag{19}$$

Using Equations (5), (18) and (19) the discrete Darcy velocity is defined as

$$v_h=-\mathbf{K}\nabla\phi_h \tag{20}$$

where K is the local permeability tensor of cell 1 and the normal flux at the left-hand side of S (Figure 6(a)) is resolved along the outward normal vector $\mathrm{d}L_{\mathrm{S}}=(\Delta y_{r_3,\mathrm{S}},-\Delta x_{r_3,\mathrm{S}})=\frac{1}{2}(\Delta y_{32},-\Delta x_{32})$ (Figure 6(b)) and is expressed in terms of the general tensor T as

$$F_{\mathrm{S}}^1=v_h\cdot\mathrm{d}L_{\mathrm{S}}=\tfrac{1}{2}(T_{11}^1\phi_\xi+T_{12}^1\phi_\eta)|_{\mathrm{S}}^1 \tag{21}$$

where it is understood that the resulting coefficients of $\frac{1}{2}(\phi_\xi,\phi_\eta)|_{\mathrm{S}}^1$ are denoted by $T_{11}|_{\mathrm{S}}^1$ and $T_{12}|_{\mathrm{S}}^2$ and are sub-cell approximations in physical space, of the general tensor components given in Equation (7) at the left-hand face of S. A similar expression for flux is obtained at the right-hand side of S from cell 2 (Figure 6(b)). Similarly, sub-cell fluxes are resolved on the two sides of the other faces at W, N and E. Flux continuity is then imposed across the cell interfaces at the specified positions N, S, E and W (Figure 6(a)) for a specified quadrature point q (Section 3.5 above). Using these positions of continuous pressure (N,S,E,W) as the flux quadrature points, and for cells 1–4 sharing a common grid vertex (Figure 6(a)), the flux continuity conditions are written as

$$\begin{aligned}
F_{\mathrm{N}}&=-\tfrac{1}{2}(T_{11}\phi_\xi+T_{12}\phi_\eta)|_{\mathrm{N}}^3=-\tfrac{1}{2}(T_{11}\phi_\xi+T_{12}\phi_\eta)|_{\mathrm{N}}^4\\
F_{\mathrm{S}}&=-\tfrac{1}{2}(T_{11}\phi_\xi+T_{12}\phi_\eta)|_{\mathrm{S}}^1=-\tfrac{1}{2}(T_{11}\phi_\xi+T_{12}\phi_\eta)|_{\mathrm{S}}^2\\
F_{\mathrm{E}}&=-\tfrac{1}{2}(T_{12}\phi_\xi+T_{22}\phi_\eta)|_{\mathrm{E}}^2=-\tfrac{1}{2}(T_{12}\phi_\xi+T_{22}\phi_\eta)|_{\mathrm{E}}^3\\
F_{\mathrm{W}}&=-\tfrac{1}{2}(T_{12}\phi_\xi+T_{22}\phi_\eta)|_{\mathrm{W}}^1=-\tfrac{1}{2}(T_{12}\phi_\xi+T_{22}\phi_\eta)|_{\mathrm{W}}^4
\end{aligned} \tag{22}$$

The above system of equation yields

$$F=A_{\mathrm{L}}\Phi_{\mathrm{f}}+B_{\mathrm{L}}\Phi_{\mathrm{v}}=A_{\mathrm{R}}\Phi_{\mathrm{f}}+B_{\mathrm{R}}\Phi_{\mathrm{v}} \tag{23}$$

where $\Phi_{\mathrm{f}}=(\phi_{\mathrm{N}},\phi_{\mathrm{S}},\phi_{\mathrm{E}},\phi_{\mathrm{W}},)$ represents interface pressures. Similarly, $\Phi_{\mathrm{v}}=(\phi_1,\phi_2,\phi_3,\phi_4,)$ represents cell-centred pressures. Thus, the four interface pressures are expressed in terms of the four cell-centred pressures. From Equation (23) Φ_{f} is eliminated to obtain the flux

coefficient matrix given as

$$F = (A_{\mathrm{L}}(A_{\mathrm{L}} - A_{\mathrm{R}})^{-1}(B_{\mathrm{R}} - B_{\mathrm{L}}) + B_{\mathrm{L}})\Phi_{\mathrm{v}} \tag{24}$$

This illustrates a key advantage of the method as in one dimension, the cell-face pressures are determined locally in terms of the cell-centred pressures in a preprocessing step, thus avoiding introduction of the interface pressure equations into the assembled discretization matrix. Therefore, flux continuity in the case of a general tensor is obtained while maintaining the standard single degree of freedom per cell. Since the continuity equations depend on both ϕ_ξ and ϕ_η (unless a diagonal tensor is assumed with cell-face mid-point quadrature resulting in a two-point flux), the interface pressures $\Phi_{\mathrm{f}} = (\phi_{\mathrm{N}}, \phi_{\mathrm{S}}, \phi_{\mathrm{E}}, \phi_{\mathrm{W}},)$ are locally coupled and each group of four interface pressures is determined simultaneously in terms of the four cell-centred pressures whose union contains the continuity positions.

3.7. Discrete flux approximation for structured grids

Once the flux coefficient matrix has been calculated (Equation (24)) the discrete scheme is defined by approximating Equation (8) with the sum of eight fluxes, two per control-volume quadrant as in Figure 7(a), the top right-hand *dual-cell* has index $i + 1/2, j + 1/2$. The net flux for the respective right-hand side and top cell faces (in a global assembly) is given by

$$\begin{aligned} F_{i+1/2,j} &= F_{\mathrm{N}_{i+1/2,j-1/2}} + F_{\mathrm{S}_{i+1/2,j+1/2}} \\ F_{i,j+1/2} &= F_{\mathrm{E}_{i-1/2,j+1/2}} + F_{\mathrm{W}_{i+1/2,j+1/2}} \end{aligned} \tag{25}$$

Finally, the discrete scheme is completed by defining the closed integral of net flux over the control-volume (i, j) which results in

$$F_{i+1/2,j} - F_{i-1/2,j} + F_{i,j+1/2} - F_{i,j-1/2} = M \tag{26}$$

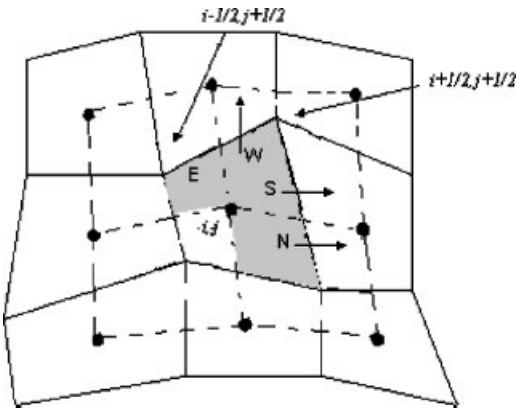

Figure 7. Control-volume quadrant fluxes on a Cartesian grid.

where M is the specified flow rate. It should also be noted here that for any quadrature point q, other than the cell-face mid-point ($q = 1$), a nine-point flux-continuous scheme is always obtained regardless of whether the tensor is full or diagonal.

3.8. Formulation in transform space

The physical space tensor resulting from normal resolution of velocity will not in general be symmetric, i.e. $T^{\mathrm{l}}_{12}|_{\mathrm{S}} \neq T^{\mathrm{l}}_{12}|_{\mathrm{W}}$, and the resulting discrete matrix is non-symmetric. Alternative formulations that yield a symmetric positive definite discrete matrix can be derived in transform space, where the local general tensor T assumes a piecewise constant approximation over the control-volume cell [1] or is piecewise constant over the sub-cells of each control-volume [6, 7]. These formulations introduce additional approximations in geometry, the latter [6, 7] are proving to introduce less error than the former, consistent with being defined on the sub-grid scale [24]. A convergence comparison between physical and transform space formulation for the former case is presented in results section and it shows that the approximation of geometry introduces a second-order error.

3.9. Formulation of scheme in physical space—unstructured grids

This section presents a brief summary of the formulation of flux-continuous schemes for unstructured grids. In this case, pressures and permeabilities are vertex centred. A control-volume is constructed around each vertex by joining cell edge mid-points to cell centres for all cells common to a given vertex. The physical permeability is assigned to the control-volume. Using an analogous procedure to that for the structured grids the flux continuity formulation is carried over directly to treat unstructured triangular grids [2]. For a triangular grid three flux continuity conditions are imposed within each triangle where a local co-ordinate system is associated with each sub-cell of a given triangle, Figure 8(a). Interface pressures $\Phi_{\mathrm{f}} = (\phi_{\mathrm{N}}, \phi_{\mathrm{S}}, \phi_{\mathrm{E}})$ are introduced in a similar fashion to Section 3.2 and three sub-cell triangular basis functions are formed joining vertex pressures $\Phi_{\mathrm{v}} = (\phi_1, \phi_2, \phi_3)$ with adjacent interface pressures Φ_{f}. The pressure assumes a piecewise linear variation over each sub-cell triangle and the derivatives ϕ_x and ϕ_y are linear functions of Φ_{f} and Φ_{v}.

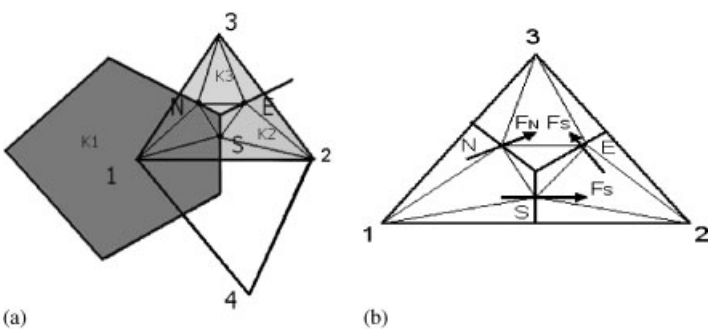

Figure 8. (a) Control-volume, flux and pressure continuity positions at N, S, E shown on a triangle, quadrature $q = 1/2$; and (b) sub-cell triangular basis functions and fluxes at interface.

3.10. Discrete flux approximation for unstructured grids

Similar to the structured case the system of fluxes for unstructured grids are rearranged in the form

$$F = A_L \Phi_f + B_L \Phi_v = A_R \Phi_f + B_R \Phi_v \tag{27}$$

where $\Phi_f = (\phi_N, \phi_S, \phi_E)$ represents the interface pressures for triangular grids. Similarly, $\Phi_v = (\phi_1, \phi_2, \phi_3)$ represents cell-vertex pressures for triangular grids. Thus, the interface pressures can now be expressed in terms of the cell-vertex pressures. From Equation (27) Φ_f can be eliminated to obtain the flux coefficient matrix as for structured grid and is given as

$$F = (A_L(A_L - A_R)^{-1}(B_R - B_L) + B_L)\Phi_v \tag{28}$$

After calculating the flux coefficient matrix the Gaussian integral of divergence over each control-volume is obtained by global flux assembly.

4. CONVERGENCE STUDY RESULTS

The aim of this study is to test the effect of quadrature point on convergence. While, numerical convergence tests in transform space have previously been performed by Edwards and Rogers in Reference [1] and Numerical convergence of MPFA O-method (default member of the family of flux-continuous schemes considered here, i.e. for $q = 1$) have also been presented by Eigestad *et al.* in Reference [14], a study of numerical convergence for the family of flux-continuous schemes in terms of a range of quadrature points has not previously been presented.

In all cases the permeability field remains fixed under grid refinement, ensuring that each problem is invariant with respect to each grid level for the convergence study.

4.1. Convergence results on structured grids

In this section, convergence study results for the family of flux-continuous schemes for a range of quadrature points are presented ($q = 0.1,\ 0.5, 0.287, 1$), where $q = 0.287$ is *Gauss quadrature point*. A numerical convergence study is performed for each of the domains illustrated in Figure 9 where subdomain $K_1, \ldots, K_4$ indicates the variation in the permeability field. The different types of grid used are shown in Figure 10. The Discrete L_2 *norm* is used to investigate pressure and velocity errors, which is defined as

$$L_2 = \left(\frac{\sum_i (A_i(p_i^{\text{analytical}} - p_i^{\text{numerical}})^2)}{\sum_i A_i} \right)^{1/2} \tag{29}$$

where A_i is the area of the grid cell i. The grid refinement levels used for the L_2 *norm* calculation were 8×8, 16×16, 32×32, 64×64 and 128×128 and were used for all test cases.

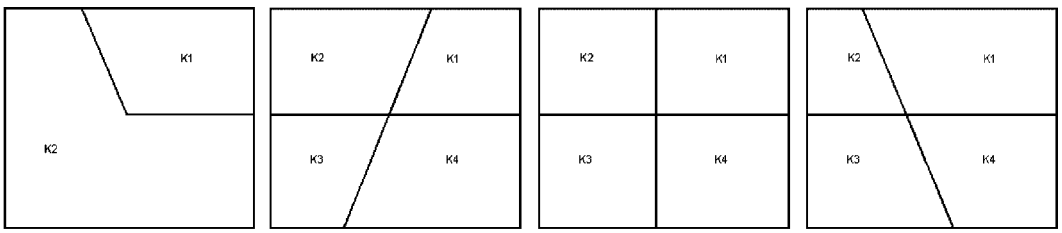

Figure 9. Different subdomains with internal discontinuous permeabilities: (a) subdomain with discontinuity along $\theta = 2\pi/3$; (b) subdomain with discontinuity along $\theta = \pi/3$; (c) subdomain with discontinuity along $\theta = \pi/2$; and (d) subdomain with discontinuity along $\theta = 2\pi/3$.

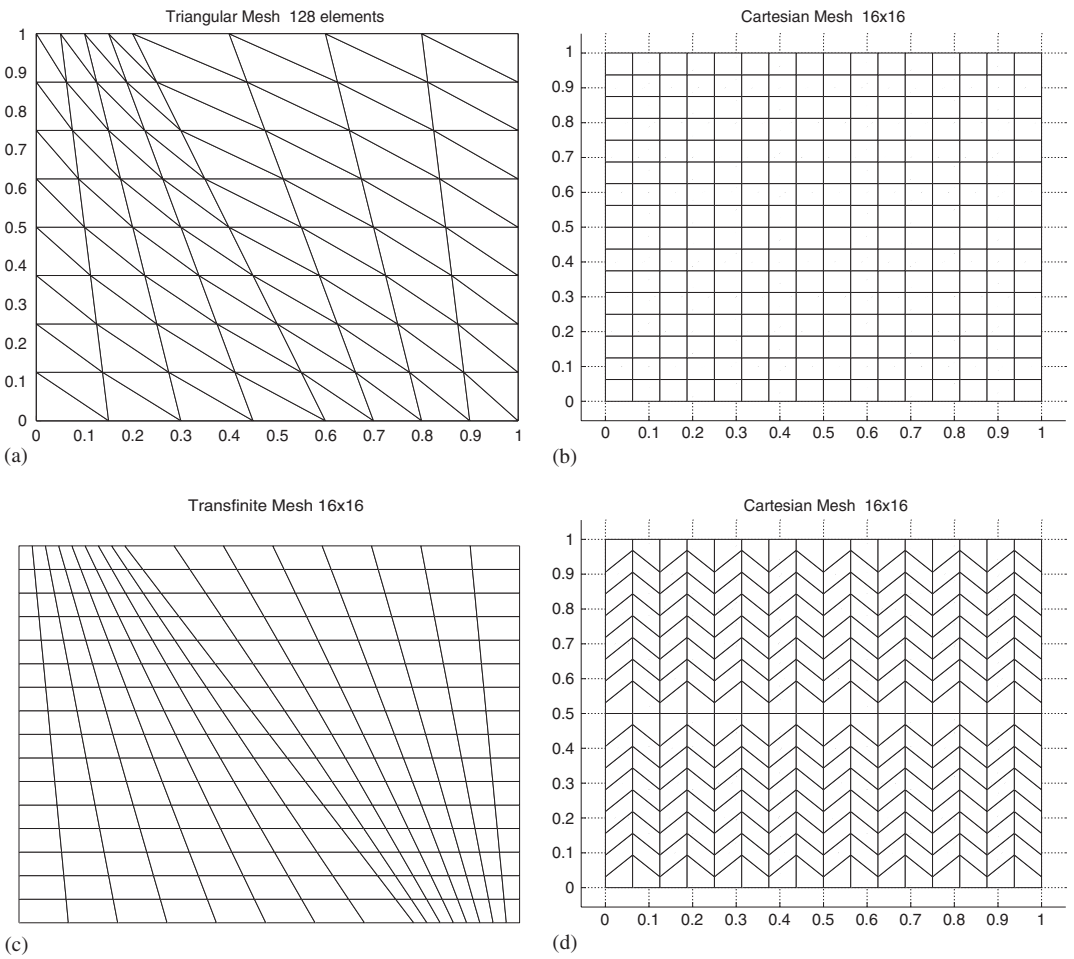

Figure 10. Different grids used to test numerical cases: (a) unstructured transfinite mesh aligned along $\theta = 2\pi/3$ discontinuity; (b) Cartesian mesh; (c) transfinite mesh aligned along $\theta = 2\pi/3$ discontinuity; and (d) zig-zag grid honouring internal discontinuity.

Example 1: The first example involves uniform flow over a rectangular domain. The medium is divided into two parts as shown is Figure 11(a). The permeability field is discontinuous and permeability ratio is 1/10 across the medium discontinuity. The discontinuity is aligned along the line $rx+sy=0$, where $r=\tan(\pi/3)/(1+\tan(\pi/3))$ and $s=1/(1+\tan(\pi/3))$. The pressure field is piecewise linear and varies as

$$\phi(x,y)=\begin{cases} rx+sy, & rx+sy<0 \\ 10(rx+sy), & rx+sy>0 \end{cases} \tag{30}$$

The diagonal permeability tensor $\mathbf{K}=c\mathbf{I}$, where $c=10$ for $rx+sy<0$ and $c=1$ for $rx+sy>0$. The numerical solution shown in Figure 11(b) was obtained using a grid aligned along the discontinuity. The numerical solution was found to be exact for any quadrature point, which is a result of using piecewise linear variation in pressure over each sub-cell and exact (physical space) geometry representation in the piecewise constant fluxes. On testing the

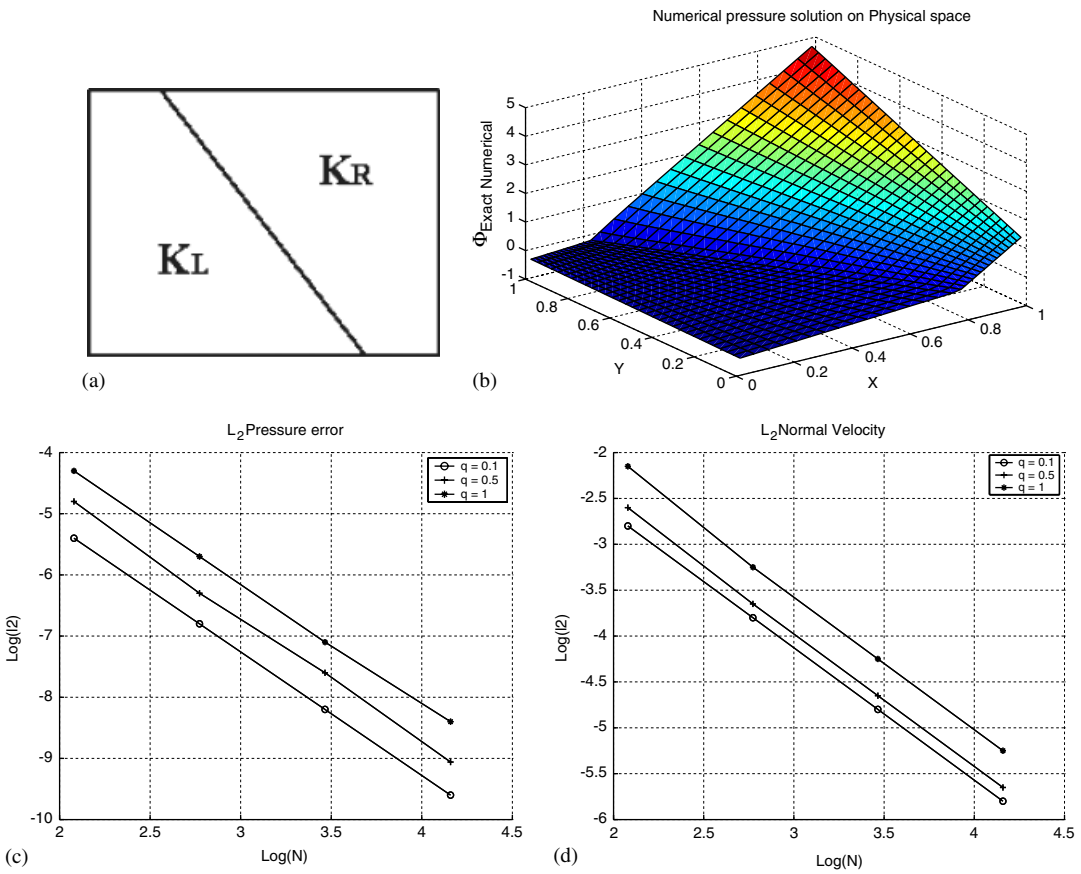

Figure 11. (a) Medium discontinuity; (b) exact numerical pressure—*physical space*; (c) numerical pressure convergence—*transform space*; and (d) numerical velocity convergence—*transform space*.

same example in transform space the order of convergence for pressure increased from $h^{1.99}$ to $h^{2.05}$ when quadrature point q moves from 1 to 0.1. The convergence rate for the normal velocity was found to be of the order of $h^{1.52}$ for $q=1$, $h^{1.5}$ for $q=0.5$ and $h^{1.45}$ for $q=0.1$. The plots of numerical convergence of pressure and normal velocity in transform space are shown in Figure 11(c) and (d). Further cases showing second-order convergence for pressure in transform space are presented in Reference [8].

We comment here that similar cases were tested by Edwards and Rogers [1] and Eigestad *et al.* [14]. Edwards and Rogers [1] obtained the exact solution for a discontinuous medium when a uniform parallelogram grid is used (where T is exact), and second-order convergence in transform space. Eigestad *et al.* used a random grid and obtained the exact solution in physical space.

The aim of this paper is to investigate convergence of flux-continuous schemes and exploit the flexibility in quadrature point by testing for a possible optimal quadrature point of the family of schemes. The above example shows that the uniform flows are reproduced exactly by the numerical scheme for any quadrature point. The following numerical examples test the numerical convergence of the family of flux-continuous schemes for a range of quadratures for more challenging examples where an exact solution is available and where the scheme cannot obtain an exact solution.

Example 2: This example is taken from Edwards and Rogers [1]. In this case, the pressure field is piecewise quadratically varying over the domain shown in Figure 12. The domain discontinuity is aligned along the line $x=1/2$, and the analytical solution is given by

$$
\begin{aligned}
\phi(x,y) &= \begin{cases} c_{\mathrm{l}}x^2 + d_{\mathrm{l}}y^2, & x<1/2 \\ a_{\mathrm{r}} + b_{\mathrm{r}}x + c_{\mathrm{r}}x^2 + d_{\mathrm{r}}y^2, & x \geqslant 1/2 \end{cases} \\
K &= \begin{cases} \begin{pmatrix} 50 & 0 \\ 0 & 1 \end{pmatrix}, & x<1/2 \\ \begin{pmatrix} 1 & 0 \\ 0 & 10 \end{pmatrix}, & x \geqslant 1/2 \end{cases} \\
\alpha &= K_{11}|_{\mathrm{r}}/K_{11}|_{\mathrm{l}} \\
\beta &= K_{22}|_{\mathrm{l}}/K_{22}|_{\mathrm{l}} \\
a_{\mathrm{r}} &= 1 \\
f &= 4a_{\mathrm{r}}/((\alpha-2)\beta+1) \\
b_{\mathrm{r}} &= (\beta-1)f \\
c_{\mathrm{r}} &= f \\
d_{\mathrm{r}} &= -c_{\mathrm{r}}K_{11}|_{\mathrm{r}}/K_{22}|_{\mathrm{r}} \\
c_{\mathrm{l}} &= \alpha\beta c_{\mathrm{r}} \\
d_{\mathrm{l}} &= d_{\mathrm{r}}
\end{aligned}
\tag{31}
$$

The imposed top boundary flux is also discontinuous at $x = 1/2$, resulting in a discontinuous tangential flux across the domain. The computed numerical solution and the plots showing L_2 norm of pressure and velocity errors for the quadrature range $(0 < q \leqslant 1)$ is shown in Figure 13. For this test case the best numerical convergence for pressure and velocity was

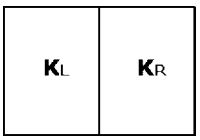

Figure 12. Discontinuous tensor field.

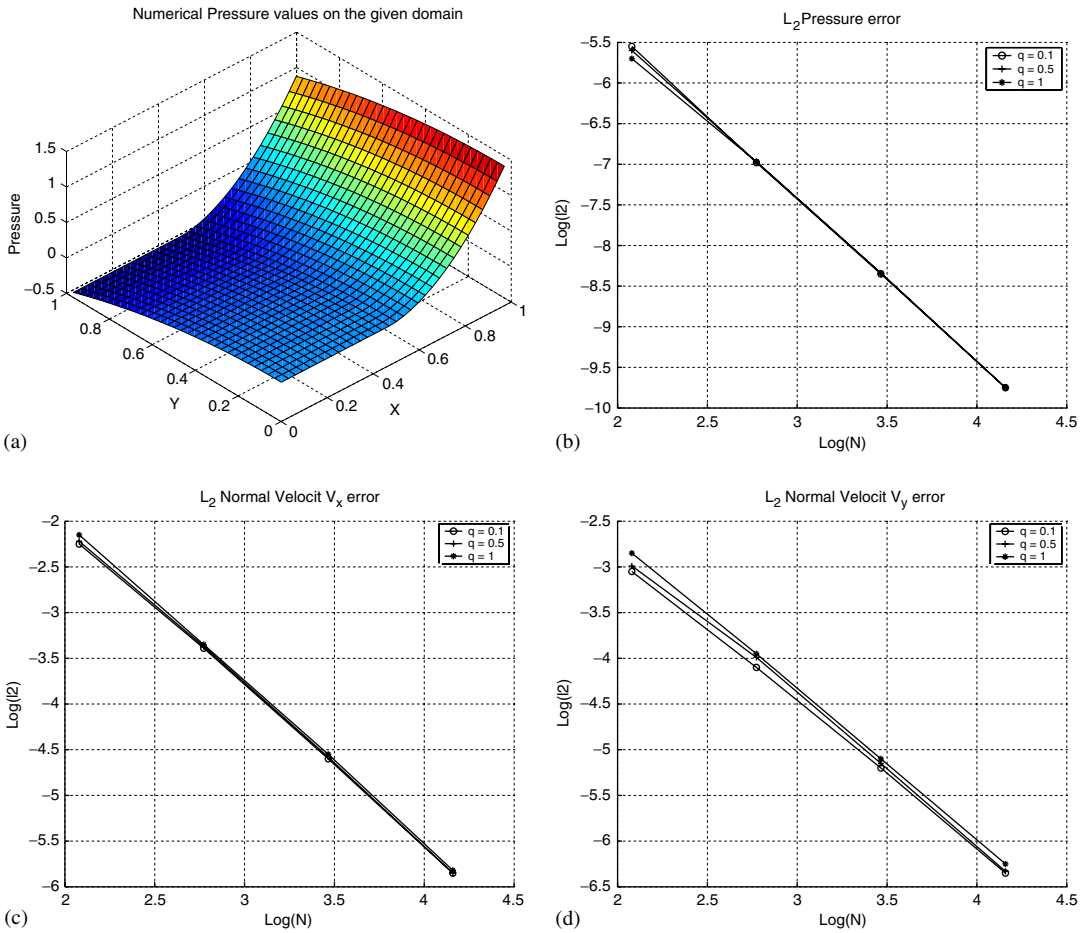

Figure 13. (a) Numerical pressure solution; (b) convergence of pressure with variable quadrature points; (c) velocity convergence of velocity along X direction; and (d) velocity convergence of velocity along Y direction.

obtained for quadrature $q=0.1$, where numerical pressure solution converges in the discrete L_2 norm with order h^2 and numerical velocity (V_x, V_y) converges with order $h^{1.77}$ and $h^{1.62}$, respectively. For quadrature point $q=0.5$ the convergence rate of pressure is found to be of the order of $h^{1.98}$ and velocity converges with the order $h^{1.77}$ and $h^{1.64}$ in X and Y directions. For quadrature point $q=1$ the convergence rate of pressure is of the order of $h^{1.95}$ and the velocity convergence with the order $h^{1.78}$ and $h^{1.68}$ in X and Y directions.

The next cases test the effect of discontinuous permeability with a corner in the field upon convergence. In each of the following examples (examples 3–7) taken from Eigestad *et al.* [14] and Riviere [25] the problem involves a rectangular domain with discontinuous permeability variation as indicated in Figure 9. The exact solution in each case takes the form

$$\phi(r,\theta)=r^{\alpha}(a_i\sin(\theta)+b_i\cos(\theta)) \tag{32}$$

Difference between problems are in terms of strength of the coefficients, permeability tensor and orientation, which also determine the level of difficulty in each case.

Example 3: For this case analytical pressure solution is given by Equation (32) and the domain discontinuity shown in Figure 9(c) has an internal angle $\theta=\pi/2$. The permeability tensor is given as $\mathbf{K}_i=k_i\mathbf{I}$ where k_i is a scalar, for $i=1,\ldots,4$, taking values $k_1=5$, $k_3=k_1$ and $k_2=1$, $k_4=k_1$. Cartesian and zig-zag grids shown in Figure 10(b) and (d) were used to test this problem. The coefficients that describe the analytical solution are given by

$$\begin{aligned}
&\alpha=0.53544095\\
&a_1=0.44721360, \quad b_1=2.33333333\\
&a_2=-0.74535599, \quad b_2=1.0\\
&a_3=-0.94411759, \quad b_3=0.5555556\\
&a_4=-2.40170264, \quad b_4=-0.481481481
\end{aligned} \tag{33}$$

The L_2 norm of pressure and velocity errors along with the numerical pressure solution obtained on a Cartesian grid are shown in Figure 14. Here, the best numerical convergence of pressure and velocity on Cartesian grid was obtained for quadrature $q=0.1$, where numerical pressure converges in the discrete L_2 norm with order $h^{1.0653}$ and numerical velocity (V_x, V_y) converges with order $h^{0.109}$ and $h^{0.12}$, respectively. For quadrature point $q=0.5$ the convergence rate for pressure is of the order of $h^{1.02}$ and the numerical convergence for velocity in X and Y direction is of the order of $h^{0.082}$ and $h^{0.081}$, respectively. The numerical convergence of pressure for quadrature $q=1$ is of the order of $h^{1.02}$ and the numerical convergence of velocity is of the order of $h^{0.068}$ and 0.063 in X and Y directions.

Using zig-zag/Chevron grids shown in Figure 10(d) the numerical pressure converges with order $h^{1.09}$ and numerical velocity converges with order $h^{0.205}$ for quadrature $q=0.1$, whereas for quadrature $q=0.5$ pressure convergence of the order of $h^{1.12}$ and velocity convergence of

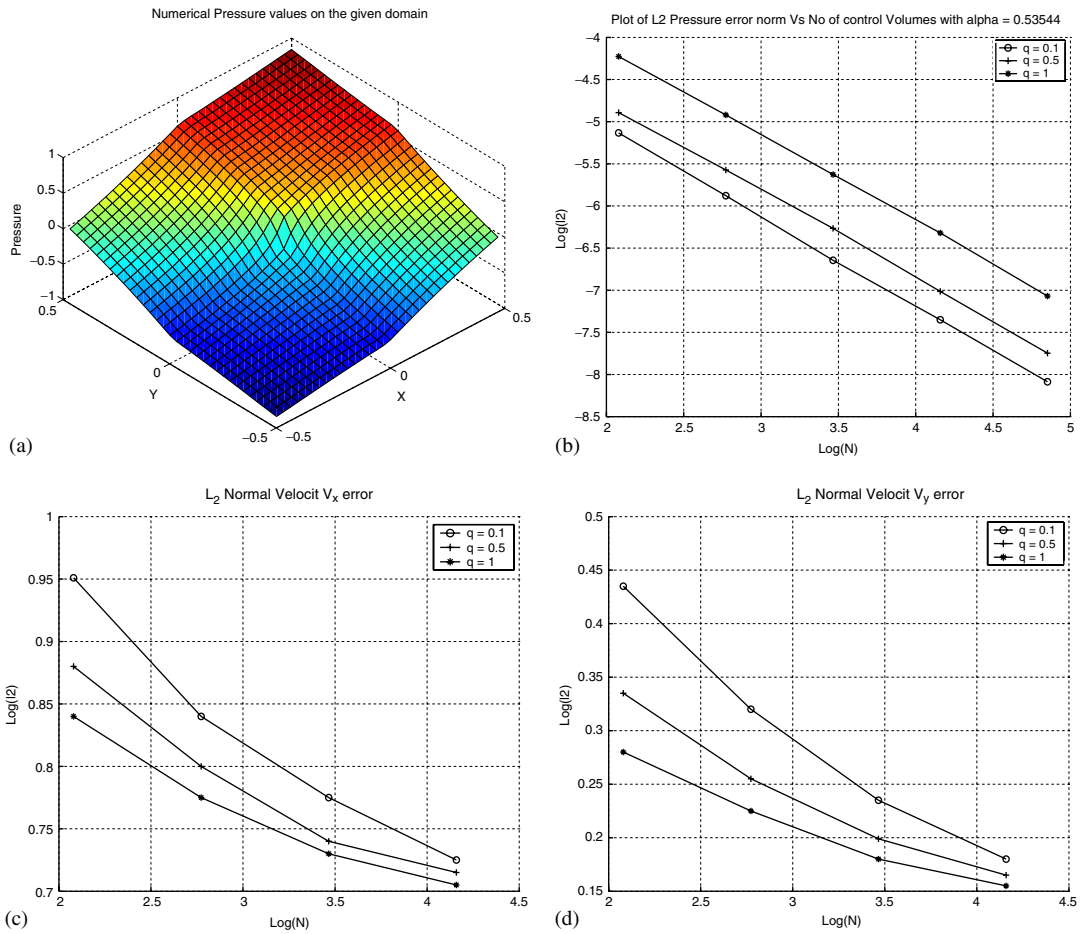

Figure 14. (a) Numerical pressure solution; (b) convergence of pressure with variable quadrature points; (c) convergence of velocity along X direction; and (d) convergence of velocity along Y direction.

the order of $h^{0.186}$ was obtained and for $q=1$ the convergence rate was found to be of the order of $h^{1.07}$ for pressure and $h^{0.175}$ for normal velocity. The plots of L_2 norm for numerical pressure and velocity errors for different quadrature points using zig-zag grids is shown in Figure 15.

Example 4: For this case analytical solution for pressure is given by Equation (32) and the domain discontinuity is shown in Figure 9(c) with an internal angle $\theta=\pi/2$. The permeability tensor is given by $\mathbf{K}_i=k_i\mathbf{I}$ where k_i is a scalar, for $i=1,\ldots,4$, taking values $k_1=100,\ k_3=k_1$ and $k_2=1,\ k_4=k_1$. This problem is tougher compared to the previous one as there a large variation in permeability across the discontinuity and α value is small comparatively. The problem is tested on Cartesian and zig-zag shown in Figure 10(b) and (d). The coefficients

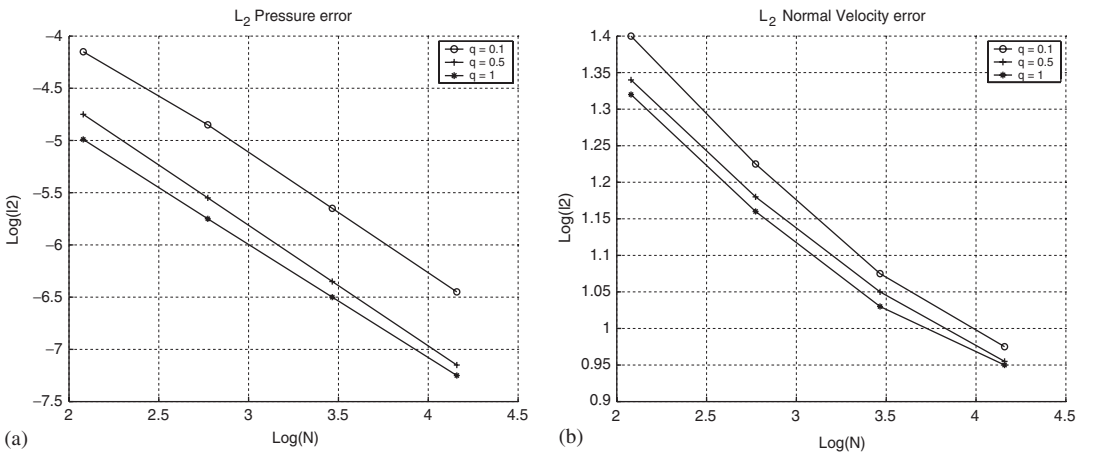

Figure 15. (a) Numerical pressure convergence with variable quadrature; and (b) numerical velocity convergence with variable quadrature.

that describe the analytical solution are given by

$$\begin{aligned} \alpha &= 0.126902097221 \\ a_1 &= 0.1, \quad b_1 = 1.0 \\ a_2 &= -9.603960396, \quad b_2 = 2.960396040 \\ a_3 &= -0.4803548672, \quad b_3 = -0.8827565925 \\ a_4 &= 7.701564882, \quad b_4 = -6.456461752 \end{aligned} \tag{34}$$

L_2 norm of pressure and velocity errors obtained on a Cartesian grid are shown in Figure 16. The best numerical convergence for pressure and velocity on a Cartesian grid was again obtained for quadrature $q = 0.1$, where numerical pressure solution converges in the discrete L_2 norm with order $h^{0.326}$ and numerical velocity (V_x, V_y) were found to be diverging. At this time, while the reason for divergence of velocity is not clear, we note that velocity is proportional to pressure gradient, and is therefore more sensitive than pressure in the presence of a singularity. The divergence of velocity is also observed by Eigestad *et al.* [14]. The convergence rate of pressure for $q = 0.5$ and 1 is of the order of $h^{0.194}$ and $h^{0.166}$, respectively. Using zig-zag/Chevron grids shown in Figure 9(d) the numerical pressure converges with order $h^{1.02}$, $h^{0.285}$ and $h^{0.287}$ for $q = 0.1$, 0.5 and 1, respectively, showing a clear advantage in pressure convergence when using $q = 0.1$. However, velocity diverges. As before, such a diverging behaviour of velocity is consistent with Eigestad *et al.* [14]. Figure 17 shows the plots of numerical pressure and velocity convergence with variable quadrature points on zig-zag grids. The pressure convergence results known for this test case from Eigestad *et al.* [14] is of the order of $h^{0.22}$.

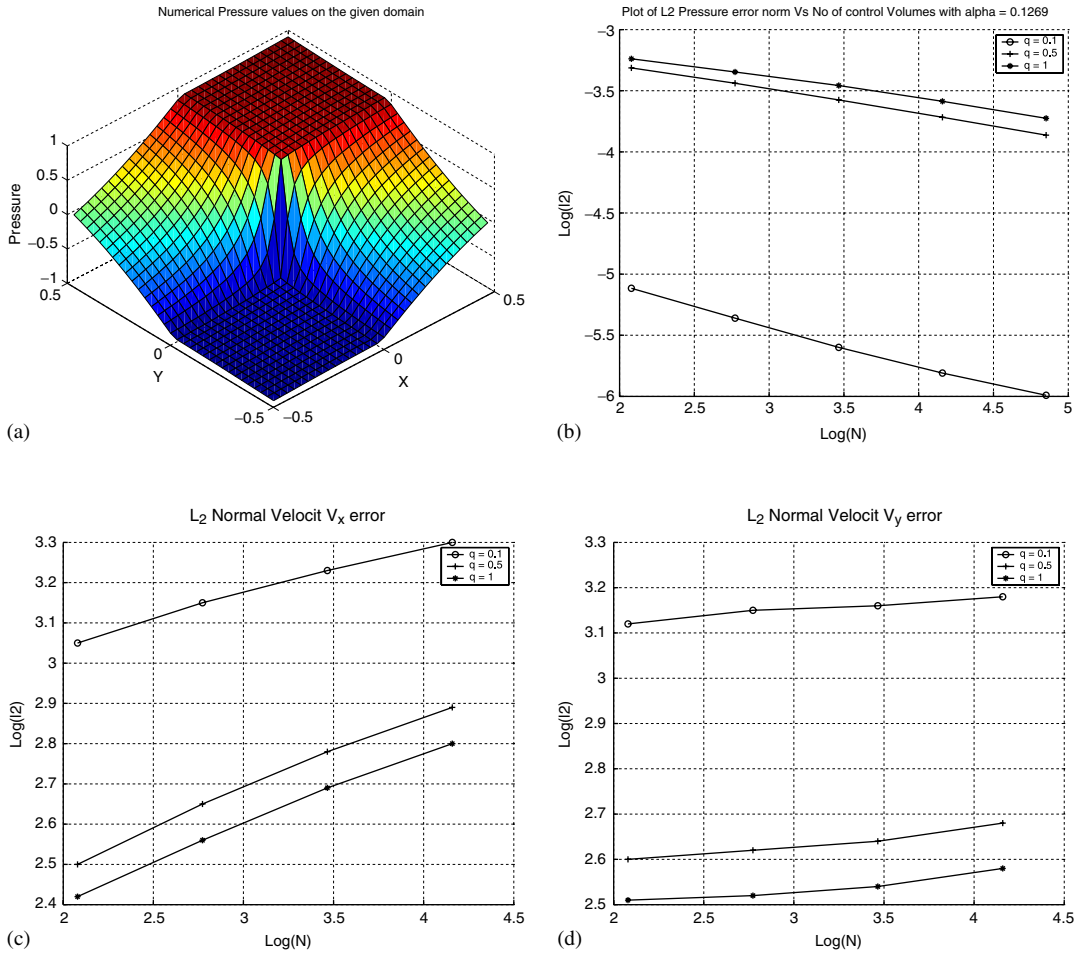

Figure 16. (a) Numerical pressure solution; (b) numerical convergence of pressure with variable quadrature points; (c) numerical convergence of velocity along X direction; and (d) numerical convergence of velocity along Y direction.

Example 5: In this case, analytical solution is given by Equation (32) and the domain discontinuity is along the line $2\pi/3$ shown in Figure 9(a). The domain is divided into two parts with the permeability tensor $\mathbf{K}_i = k_i\mathbf{I}$ where k_i is a scalar, for $i = 1, 2$ taking values $k_1 = 100$ and $k_2 = 1$. The grid used to test this case was aligned along the discontinuity. The coefficients that describes the analytical solution are given by

$$\begin{aligned} &\alpha = 0.75472745 \\ &a_1 = 1.0, \quad b_1 = 1.00995049 \\ &a_2 = 100.980198, \quad b_2 = 1.99990197 \end{aligned} \tag{35}$$

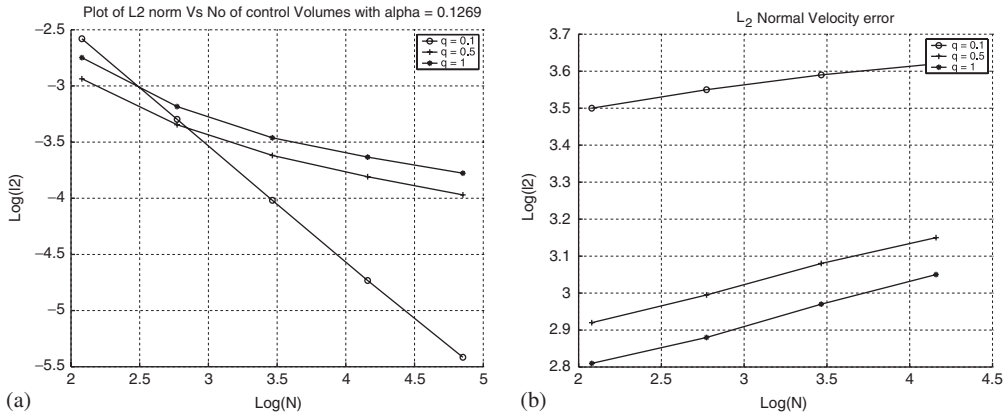

Figure 17. (a) Numerical convergence of pressure with variable quadrature; and (b) numerical convergence of velocity with variable quadrature.

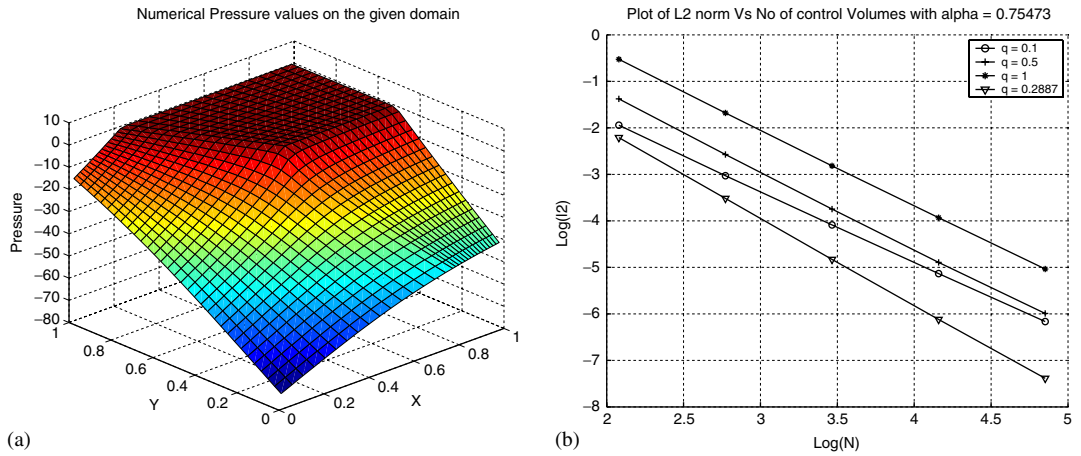

Figure 18. (a) Numerical pressure solution; and (b) numerical pressure convergence with variable quadrature.

For this test case a numerical convergence of pressure of the order is $h^{1.523}$ was obtained for quadrature point $q = 0.1$ on the grid aligned along the discontinuity. The pressure convergence for different quadrature point is shown in Figure 18. The convergence for velocity was found to be of the order of $h^{0.75}$. On using the gauss quadrature point $q = 0.2887$ the convergence rate of pressure was found to be of the order of $h^{1.87}$. It was found that gauss quadrature points sometimes perform better in the case of smoother problems.

Example 6: Here, the analytical solution is given by Equation (32) and the domain discontinuity is along the line $2\pi/3$ as shown in Figure 9(d) with the permeability tensor $\mathbf{K}_i = k_i\mathbf{I}$

where k_i is a scalar, for $1,\ldots,4$, taking values $k_1 = 100$, $k_3 = k_1$ and $k_2 = 1$, $k_4 = k_1$. The grids used to test this case were aligned along the discontinuity. The coefficients that describe the analytical solution are given by

$$\begin{aligned} &\alpha = 0.13448835 \\ &a_1 = 1.0, \quad b_1 = 0.14177447 \\ &a_2 = 4.90138222, \quad b_2 = -13.3407815 \\ &a_3 = -0.85392910, \quad b_3 = -0.53935618 \\ &a_4 = -9.94074425, \quad b_4 = 10.1578346 \end{aligned} \tag{36}$$

The plots in Figure 19(a) and (b) show the pressure errors and pressure convergence, respectively, for this test case. The pressure convergence for this test case with the grid aligned along the discontinuity was of the order of $h^{1.23}$ for quadrature $q = 0.1$. The reported convergence of pressure for this test case in Reference [14] was of the order of $h^{0.24}$. This result again demonstrates that a significant improvement in convergence is obtained by exploiting the family of schemes and using the quadrature point $q = 0.1$. This case is not as smooth as the previous one and on using gauss quadrature point $q = 0.2887$ the convergence of pressure for this case was found to be of the order of $h^{0.43}$ which is less than convergence rate found for $q = 0.1$.

Example 7: Here, the analytical solution for pressure is also given by Equation (32) and the domain discontinuity is along the line $\pi/3$ as shown in Figure 9(b) with the permeability tensor $\mathbf{K}_i = k_i\mathbf{I}$, where k_i is a scalar, for $1,\ldots,4$, taking values $k_1 = 6$, $k_3 = k_1$ and $k_2 = 1$, $k_4 = k_1$. The grids used to test this were aligned along the discontinuity. The coefficients that describe

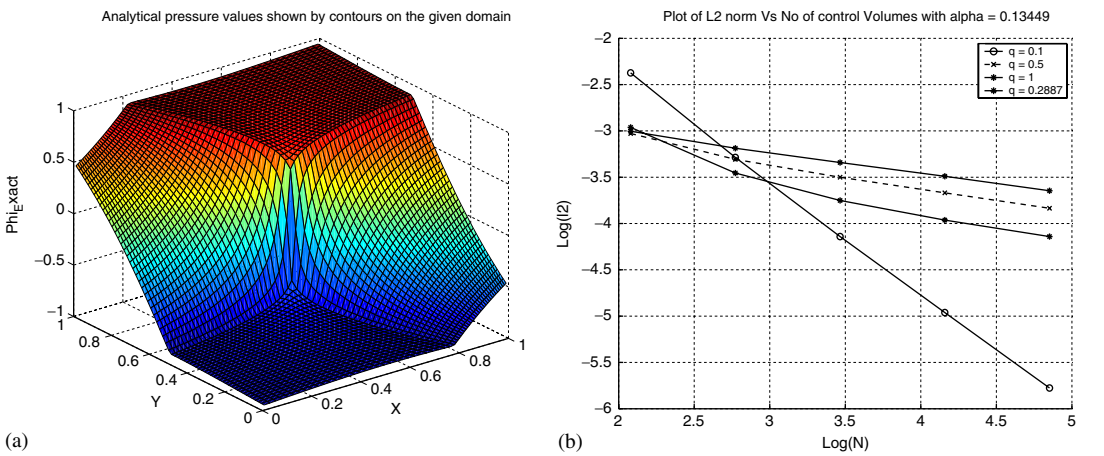

Figure 19. (a) Numerical pressure on the given domain; and (b) convergence of numerical pressure for different quadrature points.

the analytical solution are given by

$$\begin{aligned} \alpha &= 0.51671199 \\ a_1 &= 1.0, \quad b_1 = 0.27735010 \\ a_2 &= 1.71428571, \quad b_2 = -0.91129318 \\ a_3 &= 0.32944606, \quad b_3 = -0.98406726 \\ a_4 &= -0.820074971, \quad b_4 = -1.75974652 \end{aligned} \tag{37}$$

The plots in Figure 20(a) and (b) show the numerical pressure solution and pressure convergence, respectively, for this test case. The pressure convergence for this test case with the grid aligned along the discontinuity was of the order of $h^{1.051}$ for quadrature $q = 0.1$ and the velocity convergence was found to be of the order of $h^{0.52}$.

A series of other numerical examples were also tested on Cartesian and zig-zag grids with different values of α, a_i and b_i over the domains shown in Figure 9(b)–(d). All show the same trend, i.e. for quadrature point $q = 0.1$ convergence results are the best compared to other quadrature points.

4.2. *Convergence results on unstructured grids*

In this section, the family of flux-continuous schemes is tested on an unstructured grid. This test case is taken from Edwards and Rogers [1]. For this case the permeability is discontinuous with a domain discontinuity similar to the one shown in example 1 and is given along the line $x + y/2 = 3/4$. The grid used for solving the unstructured case is control-volume aligned

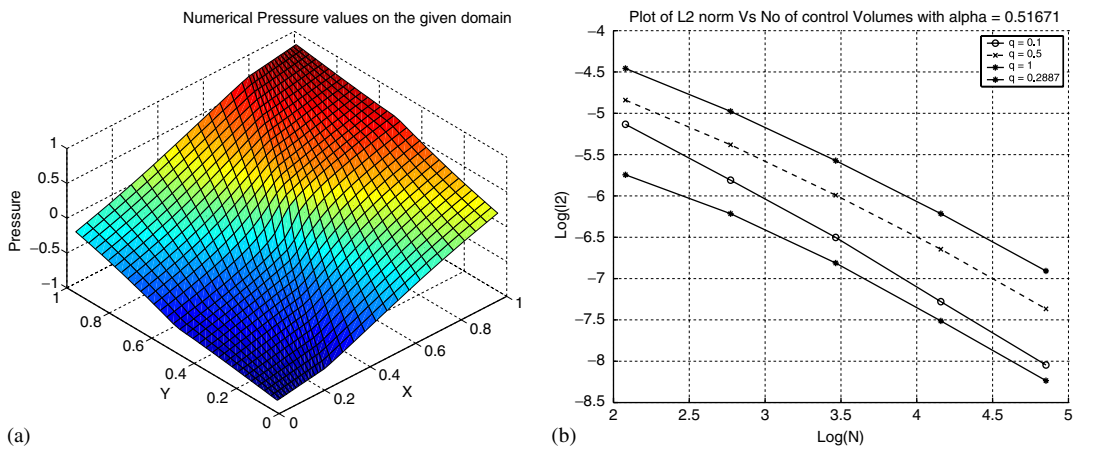

Figure 20. (a) Numerical pressure solution; and (b) numerical convergence of pressure with variable quadrature points.

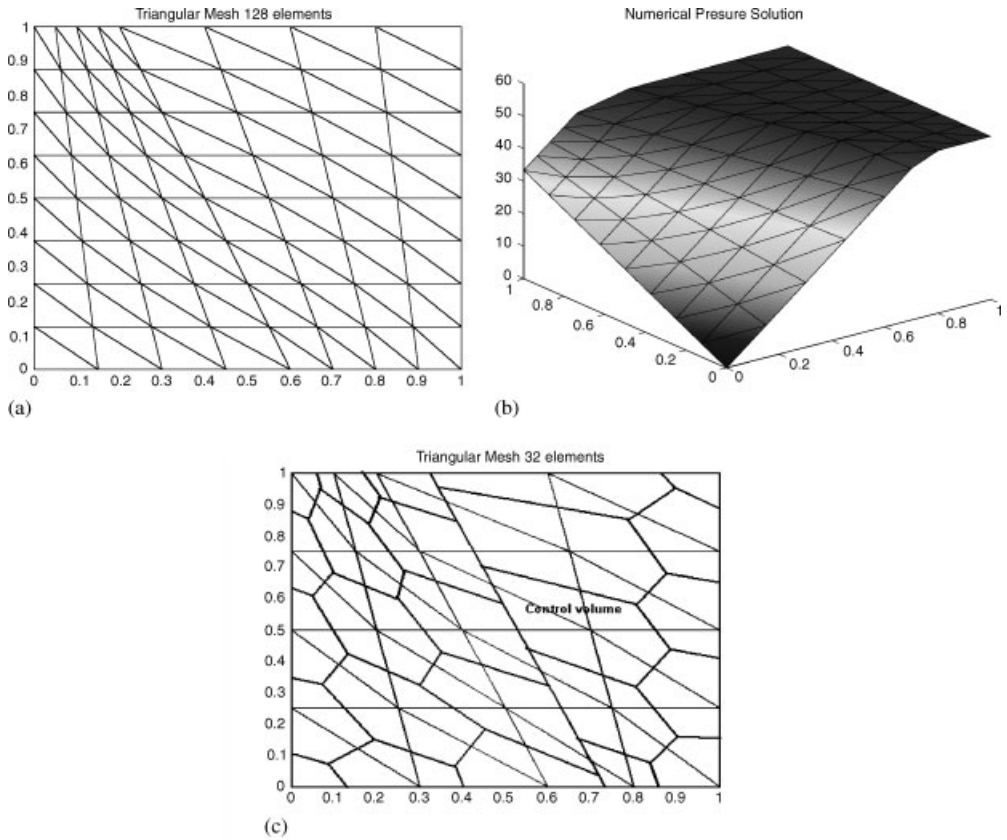

Figure 21. (a) Unstructured grid; (b) exact numerical solution; and (c) control-volume aligned triangular grid.

as shown in Figure 21(c). The pressure field is piecewise linear and is given by

$$\phi(x,y)=\begin{cases}200/3(x+y/2), & x+y/2<3/4\\ 2/3(x+y/2)+99/2, & x+y/2\geqslant 3/4\end{cases} \tag{38}$$

A full discontinuous permeability tensor is defined as

$$K=\begin{cases}\begin{pmatrix}1 & -1/4\\ -1/4 & 1/2\end{pmatrix}, & x+y/3<3/4\\ \begin{pmatrix}100 & -100/4\\ -100/4 & 100/2\end{pmatrix}, & x+y/2\geqslant 3/4\end{cases}$$

On solving this problem on a unstructured grid with 128 elements shown in Figure 21(a) the exact solution shown in Figure 21(b) was obtained using the physical space formulation

for all quadrature points. This verifies that the family of flux-continuous schemes is equally applicable to unstructured grids and is exact for linear problems.

5. USE OF QUADRATURE POINT IN UP-SCALING

Up-scaling of fine scale information to the coarse (gridblock) scale is commonly performed in reservoir simulation [5]. The grid block domain is represented by a fine scale grid over which fine scale rock properties are defined and standard up-scaling is performed over the domain. In this section, an example is presented demonstrating the effect of different quadrature points on up-scaling. In this example, the fine scale permeability field is defined by four different values of diagonal permeability tensor

$$K = C_j \begin{pmatrix} 1 & 0 \\ 0 & 1 \end{pmatrix}$$

where $C_j = (0.01, 1, 0.1, 100)$ arranged in a 2×2 configuration (Figure 22). The standard effective permeability is computed for the successive grid refinements using a range of quadrature points. The domain is subjected to no flow top and bottom (Neumann) boundary conditions, i.e. $\mathbf{u} \cdot \mathbf{n}_1 = 0$ and $\mathbf{u} \cdot \mathbf{n}_2 = 0$ (typical boundary conditions for up-scaling). Dirichlet boundary conditions are applied to the left and right-hand side of the domain where constant pressures are prescribed such that a global pressure difference is imposed across the domain. A reference solution is computed on a structured 128×128 Cartesian grid. Convergence rates in terms of effective permeability $K^\star$ is shown in Figure 21. For the family of flux-continuous schemes use of quadrature point $q = 0.1$ yields the best performance. The standard CVFE (FEM-Galerkin) is computed for up-scaling subjected to same boundary conditions. FEM-GAL is seen to converge from above (Figure 23(a)) and the family of flux-continuous scheme convergence from below, consistent with harmonic mean up-scaling. A similar problem is tested on unstructured grid and the up-scaling convergence of $K^\star$, obtained in that case is shown in Figure 23(b). Again we observed the same trend that quadrature $q = 0.1$ yields improved convergence for up-scaling compared to other quadrature points including unstructured grids.

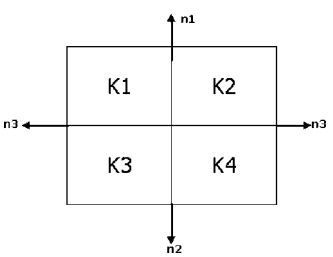

Figure 22. Domain to be up-scaled with varying permeability.

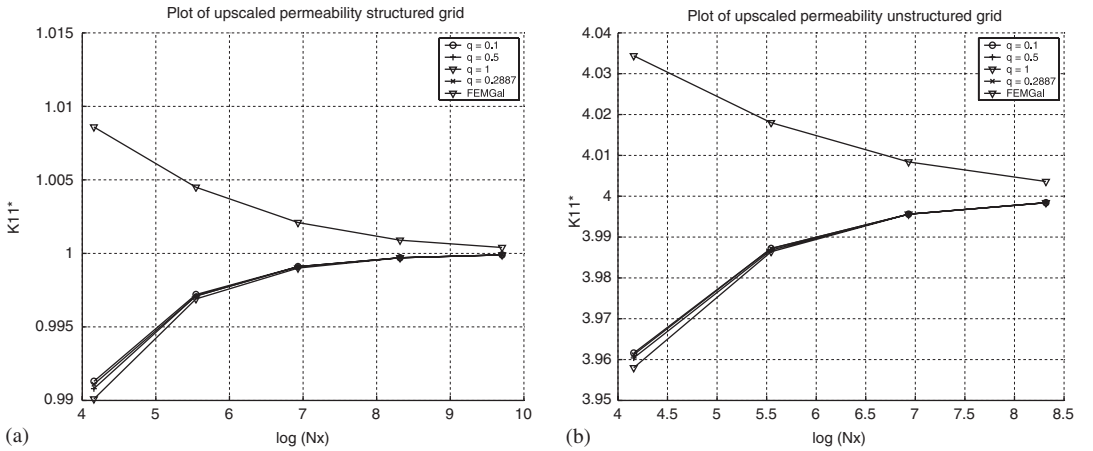

Figure 23. (a) Up-scaled permeability on structured grid; and (b) up-scaled permeability on unstructured grid.

6. CONCLUSIONS

The family of flux-continuous schemes is shown to be exact on structured and unstructured grids (for all quadrature points) for problems where pressure is piecewise linear.

For the transform space formulation $O(h^2)$ convergence is obtained for the problems where pressure is piecewise linear and thereby provides a measure of the transform space geometry approximation error.

More generally, for the cases involving an interior field singularity where pressure is expressed in polar form as a function of α it was found that convergence rate for pressure and velocity decreases with decreasing α. The numerical experiments show that there is a certain inverse proportionality between convergence rate and roughness of the coefficients, smoother coefficients tend to yield better convergence, as the coefficient of roughness increases the convergence rate decreases. However, from the convergence study it is observed that quadrature point $q = 0.1$ appears to be optimal and results in improved convergence compared to other quadrature points tested. In particular, significant improvement in convergence rates are obtained for $q = 0.1$ compared to standard MPFA ($q = 1$). This observation is substantiated further by performing a convergence study with respect to a standard up-scaling procedure on structured and unstructured grids.

ACKNOWLEDGEMENTS

The authors would like to thank ExxonMobil Upstream Research Company for supporting this project and permission to publish this paper. The work of the second author was supported in part by EPSRC grant GR/S70968/01.

REFERENCES

1. Edwards MG, Rogers CF. Finite volume discretization with imposed flux continuity for the general tensor pressure equation. *Computers and Geosciences* 1998; **2**:259–290.

2. Edwards MG. Unstructured, control-volume distributed, full-tensor finite volume schemes with flow based grids. *Computers and Geosciences* 2002; **6**:433–452.
3. Edwards MG. Simulation with a full-tensor coefficient velocity field recovered from a diagonal tensor solution. *SPE Journal* 2000; **5**:387–393.
4. Edwards MG. *M*-matrix flux splitting for general full tensor discretization operators on structured and unstructured grids. *Journal of Computational Physics* 2000; **160**:1–28.
5. Edwards MG. Superconvergent renormalization and tensor approximation. *Paper Presented at the 5th ECMOR*, Leoben, Austria, 3–6 September 1996.
6. Edwards MG. *Symmetric Positive Definite General Tensor Discretization Operator on Unstructured and Flow Based Grids. 8th European Conference on Mathematics of Oil Recovery*, Freiberg, Germany, 3–6 September 2002.
7. Edwards MG. Control-volume distributed sub-cell flux schemes for unstructured and flow based grids. *SPE Reservoir Simulation Symposium*, Houston, Texas, U.S.A., 3–5 February 2003.
8. Lamb AR. Convergence study of a family of nine-point flux continuous, finite volume schemes for the general tensor pressure equation. *MSc Thesis*, University of Wales, Swansea, 2004.
9. Aavatsmark I, Barkve T, Bøe Ø, Mannseth T. Discretization on non-orthogonal, quadrilateral grids for inhomogeneous, anisotropic media. *Journal of Computational Physics* 1996; **127**:2–14.
10. Aavatsmark I, Barkve T, Bøe Ø, Mannseth T. Discretization on unstructured grids for inhomogeneous, anisotropic media. Part I: Derivation of the methods. *SIAM Journal on Scientific Computing* 1998; **19**:1700–1716.
11. Aavatsmark I, Barkve T, Bøe Ø, Mannseth T. Discretization on unstructured grids for inhomogeneous, anisotropic media. Part II: Discussion and numerical results. *SIAM Journal on Scientific Computing* 1998; **19**:1717–1736.
12. Aavatsmark I. Introduction to multipoint flux approximation for quadrilateral grids. *Computers and Geosciences* 2002; **6**:405–432.
13. Eigestad GT, Aadland T, Asvatsmark I, Klausen RA, Nordbotten JM. Recent advances in MPFA methods. *9th European Conference on the Mathematics of Oil Recovery-Cannes*, France, 30 August–2 September 2004.
14. Eigestad GT, Klausen RA. On the convergence of the multi-point flux approximation *O*-method: numerical experiments for discontinuous permeability. *Numerical Methods for Partial Differential Equations* 2005; **21**(6):1079–1098.
15. Lee SH, Jenny P, Tchelepi HA. A finite-volume method with hexahedral multiblock grids for modeling flow in porous media. *Computers and Geosciences* 2002; **6**:353–379.
16. Verma S. Flexible grids for reservoir simulation. *Ph.D. Thesis*, Stanford University, June 1996.
17. Russell TF. Relationships among some conservative discretization methods. In *Numerical Treatment of Multiphase Flows in Porous Media*, Chen Z *et al.* (eds), Lecture Notes in Physics, vol. 552. Springer: Heidelberg, 2000; 267–282.
18. Arbogast T, Wheeler MF, Yotov I. Mixed finite elements for elliptic problems with tensor coefficients as cell centered finite differences. *SIAM Journal on Numerical Analysis* 1997; **34**(2):828–852.
19. Russell TF, Wheeler WF. Finite element and finite difference methods for continuous flows in porous media. In *Mathematics of Reservoir Simulation* (Chapter 2), Ewing RE (ed.), Frontiers in Applied Mathematics. SIAM: Philadelphia, PA, 1983; 35–106.
20. Durlofsky LJ. A triangle based mixed finite element finite volume technique for modeling two phase flow through porous media. *Journal of Computational Physics* 1993; 252–266.
21. Riviere B, Wheeler MF, Banas K. Discontinuous Galerkin method applied to a single phase flow in porous media. *Computers and Geosciences* 2000; **49**:337–341.
22. Edwards MG. Cross flow tensor and finite volume approximation with by deferred correction. *Computer Methods in Applied Mechanics and Engineering* 1998; **151**:143–161.
23. Aziz K, Settari A. *Petroleum Reservoir Simulation*. Applied Science Publishers: London, 1979.
24. Edwards MG, Pal M. Symmetric positive definite pressure equation discretization and a family of sub-cell flux-continuous CVD schemes on cell centred quadrilateral grids. *IJNMF*, submitted.
25. Riviere B. Discontinuous Galerkin method for solving the miscible displacement problem in porous media. *Ph.D. Thesis*, The University of Texas at Austin, 2000.

